Supporting Information

Hierarchical hollow Ni/γ-Al_2O_3 catalyst derived from flower-like Ni-Al layered double hydroxide with stable catalytic performance for CO_2 methanation

Chengxiong Dang, [a,*] Jingxun Zhou, [a] Huanhuan Xia, [a] Weiquan Cai, [a, *]

[a] *School of Chemistry and Chemical Engineering, Guangzhou University, Guangzhou, 510006, China*

[*] To whom correspondence should be addressed.
cxdang@gzhu.edu.cn (CX Dang); cccaiwq@gzhu.edu.cn (WQ Cai), Tel: +86 20 3936 6905;

Characterization techniques

The phase structures presented in the sample were identified by X-ray diffraction (XRD, PANalytical X'pert) with Cu Kα radiation. N_2 physisorption experiments (ASAP 2460, Micromeritics) were applied to study the textural properties of the samples (surface area, pore size and pore volume). Inductively coupled plasma-optical emission spectrometer (ICP-OES) was carried out on an Agilent 5110 instrument to acquire the actual content of Ni in the sample. The Raman patterns were recorded on a Raman spectrometer (HORIBA LabRAM HR Evolution) with a 532 nm He-Ne laser as an excitation source.

Temperature-programmed reduction of hydrogen (H_2-TPR) was performed on a Xianquan TP-5080 adsorption apparatus. The samples (ca. 10 mg) were pretreated in 30 Nml/min N_2 at 300 °C for 1 h. Afterward, 10 vol % of H_2/N_2 (300 Nml/min) was applied with the temperature being increased from RT to 900 °C at a rate of 10 °C min^{-1}.

The morphologies of the samples were evaluated via scanning electron microscopy (SEM, Hitachi SU8220), while the elemental composition was obtained from Energy Dispersive X-ray spectroscopy (EDX). Transmission electron microscopy (TEM) images were recorded in a FEI TalosF200x field emission transmission electron microscope operated at 200 kV. Typically, the powder sample was dispersed into ethanol under ultrasonic conditions, then dropped onto the ultra-thin carbon films and dried naturally.

The catalytic mechanism of CO_2 methanation was revealed by the *in situ* diffuse reflectance infrared Fourier-transform spectra (DRIFTS) experiments. The DRIFTS tests were performed on a Thermo Scientific Nicolet 6700 Fourier transform infrared (FT-IR) spectrometer equipped with a mercury-cadmium-tellurium A (MCT/A) detector and a PIKE DiffusIR™ diffuse reflectance (DR) accessory. All gases used for *in situ* DRIFTS experiments, i.e., He (99.9999%), H_2 (99.9999%), CO_2 (5%, balanced with He, 99.99%), were supplied by Air Liquide, and further purified by additional moisture traps (BMT-2, Agilent). Each gas flow rate was precisely controlled by corresponding mass flow controller (Sevenstar), and then mixed with other gases under a controlled composition into the sample cell. The FT-IR spectrometer and the DR accessory were purged by N_2 at a typical flow rate of 10 NL/min (SLM). The DRIFT spectra were recorded from 650 to 4000 cm^{-1} at a resolution of 4 cm^{-1}, and each spectrum took 32 scans to be recorded. The integrated absorbance (***A***) was calculated using the Ominc software by baseline to baseline integration of the DRIFT spectra in the specified region.

In a typical experiment, Ni/H-γ-Al_2O_3 catalyst (*ca*. 10 mg) was first loaded into a cylindrical porous sample holder (4 mm I.D.) and then placed into the sample cell, which was subsequently sealed by a threaded stainless-steel disk installed with a KBr window. H_2 flow (5 Nml/min) was introduced to the sample cell to reduce Ni/H-γ-Al_2O_3 catalyst at a heating rate of 25 ^oC min^{-1} to 500 ^oC for 2h. Then, the H_2 flow was switched to He flow at 500 °C for another 2 h to remove the residual H_2. Prior to spectral acquisition, the sample cell was cooled down to the desired temperature in He

flow (5 Nml/min) and kept for 1 h, and the background spectrum was recorded. After switching to the gas flows (12 Nml/min) of H_2 (12.5 vol.%) and CO_2 (3.125 vol.%) balanced with He, the DRIFT spectra were obtained every 30 s for a desired period of time.

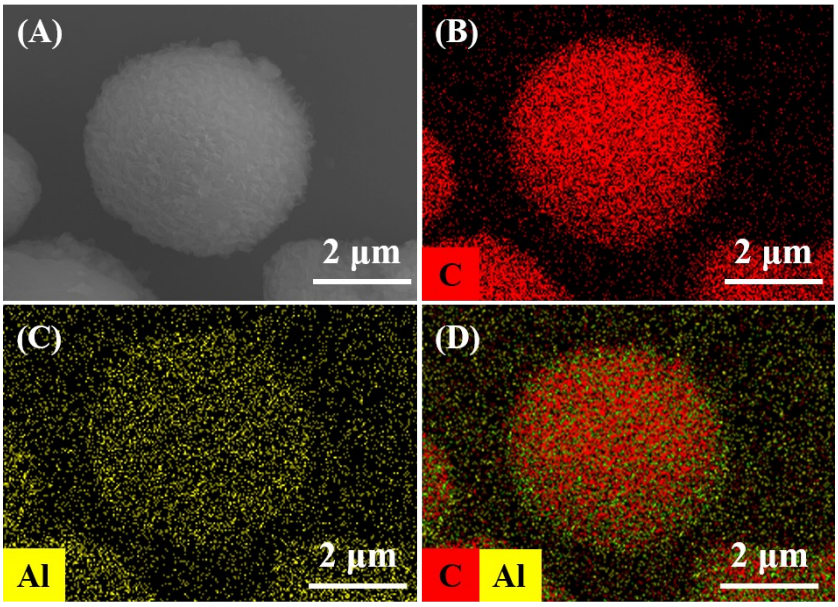

Figure S1. (A) SEM image and (B-D) EDS-mapping of the CS@γ-AlOOH sample.

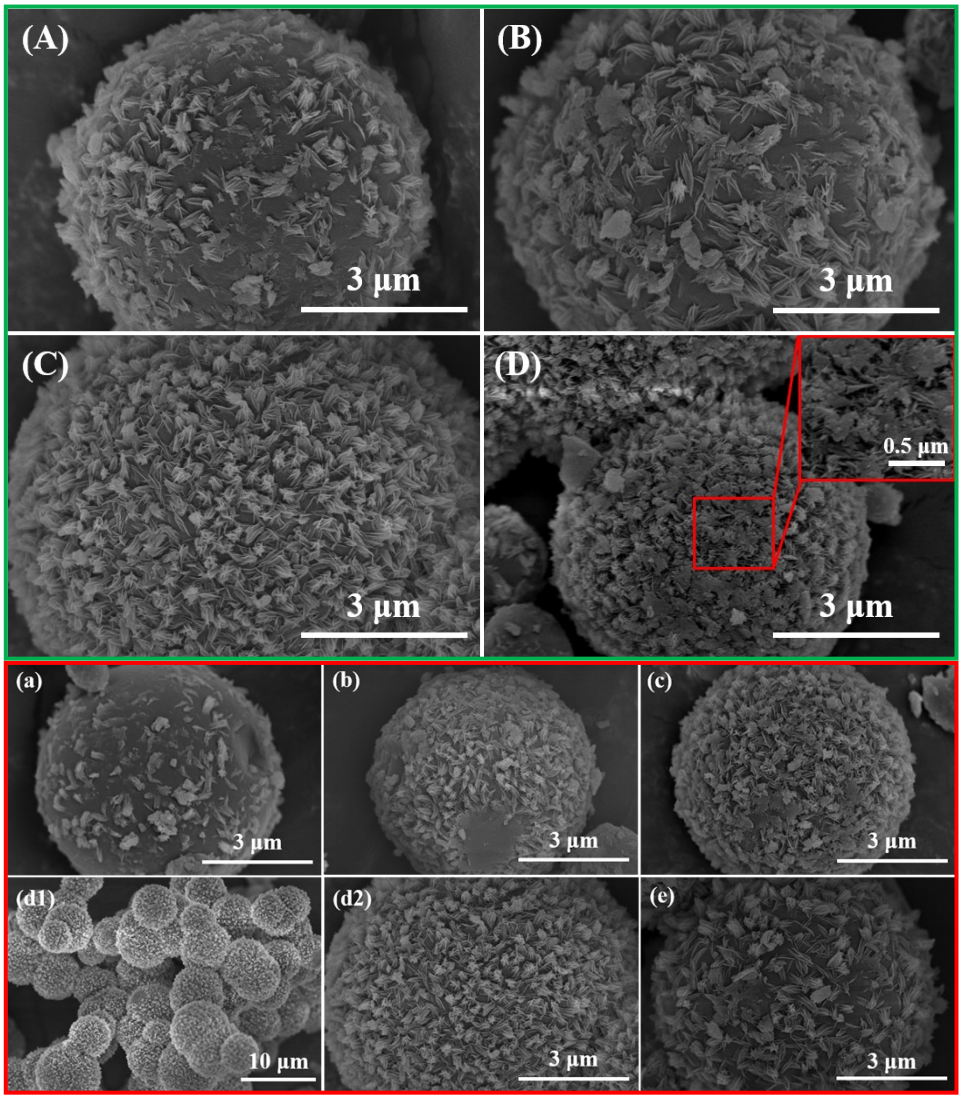

Figure S2. Effect of alkalinity on the CS@γ-AlOOH: (A) 0.42 mL, (B) 0.63 mL, (C)

0.84 mL, and (D) 1.68 mL; Effect of hydrothermal time on the CS@γ-AlOOH: (a) 6 h, (b) 12 h, (c) 18 h, (d1-d2) 24 h, and (e) 36 h.

The alkalinity of solution plays an important role in Al^{3+} precipitation, which can be afforded by the formamide (as precursor of ammonia precipitant) content. Effect of the alkalinity on the formation of the CS@γ-AlOOH was investigated (**Figure S2**). Only a few γ-AlOOH arrays exist on the surface of CS (**Figure S2(A)**) when the formamide content is low, which suggests that weak alkalinity is not favored for Al^{3+} precipitation. With the increase of alkalinity, more γ-AlOOH arrays are found on the CS (**Figure S2(B)**). Further, γ-AlOOH arrays completely cover the CS in case of suitable alkalinity with 0.84 mL of formamide as shown in **Figure S2(C)**. However, when the alkalinity continues to increase, the morphology of γ-AlOOH arrays is damaged, which may be due to the exfoliation or dissolution of γ-AlOOH in strong alkalinity. The hydrothermal time is another important factor affecting the formation of the CS@γ-AlOOH. A volcano dependence of the morphology of γ-AlOOH arrays as a function of the hydrothermal time is observed in **Figure S2(a-e).** The bushiest γ-AlOOH arrays are formed on the surface of CS with 24 h of hydrothermal time, which is attributed to the most suitable alkalinity caused by formamide hydrolysis during matched hydrothermal time. The optimal γ-AlOOH skeletons are beneficial for the highly homogeneous dispersion of Ni species in LDH by a in situ synthetic method. It is concluded that the amount and morphology of γ-AlOOH arrays are strongly dependent on the alkalinity of solution, which is regulated by the formamide content and time during the hydrothermal process.

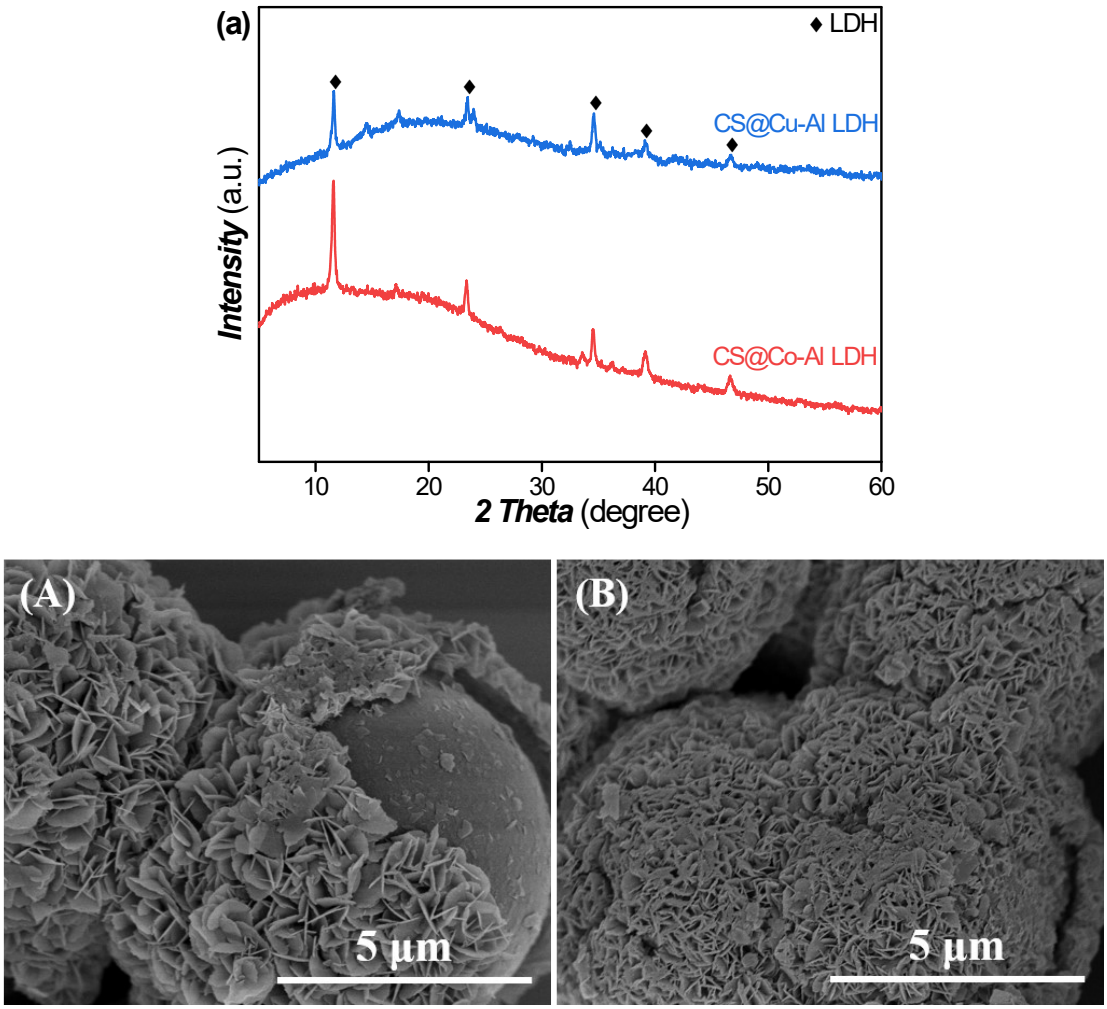

Figure S3. XRD patterns of the CS@Co-Al and CS@Cu-Al LDH samples and SEM images of (A) CS@Co-Al LDH and (B) CS@Cu-Al LDH.

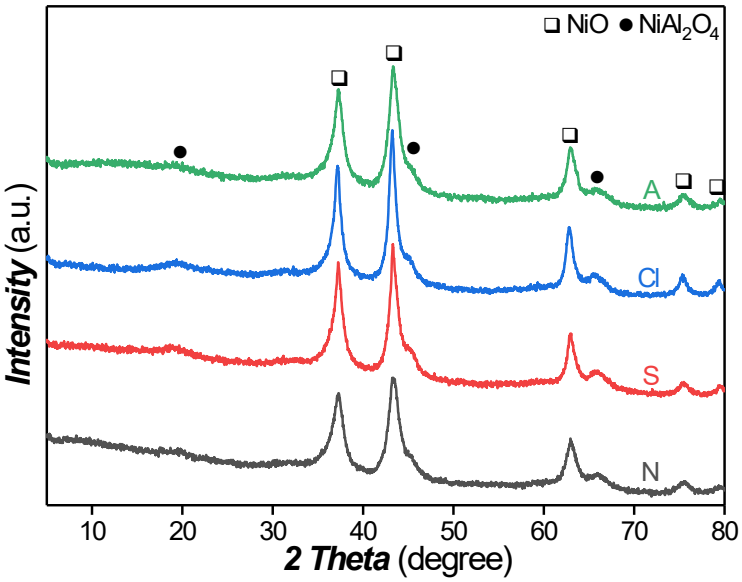

Figure S4. XRD patterns of the Ni-Al LDO-X (X: N, S, Cl, and A) samples produced by the different Ni salts.

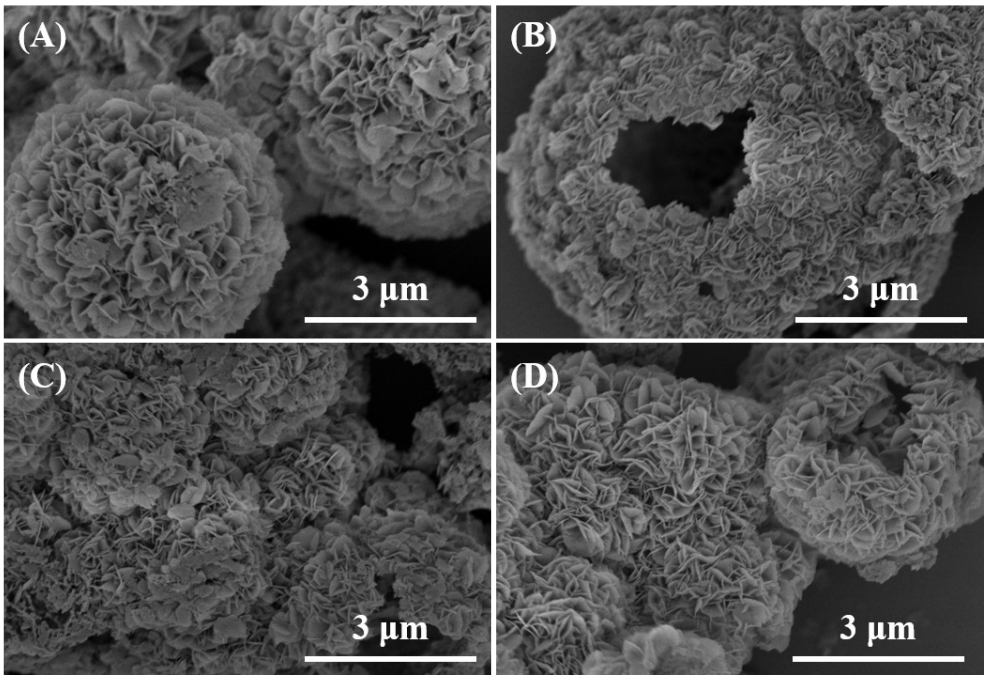

Figure S5. SEM images of (A) Ni-Al LDO-N, (B) Ni-Al LDO-S, (C) Ni-Al LDO-Cl, and (D) Ni-Al LDO-A samples.

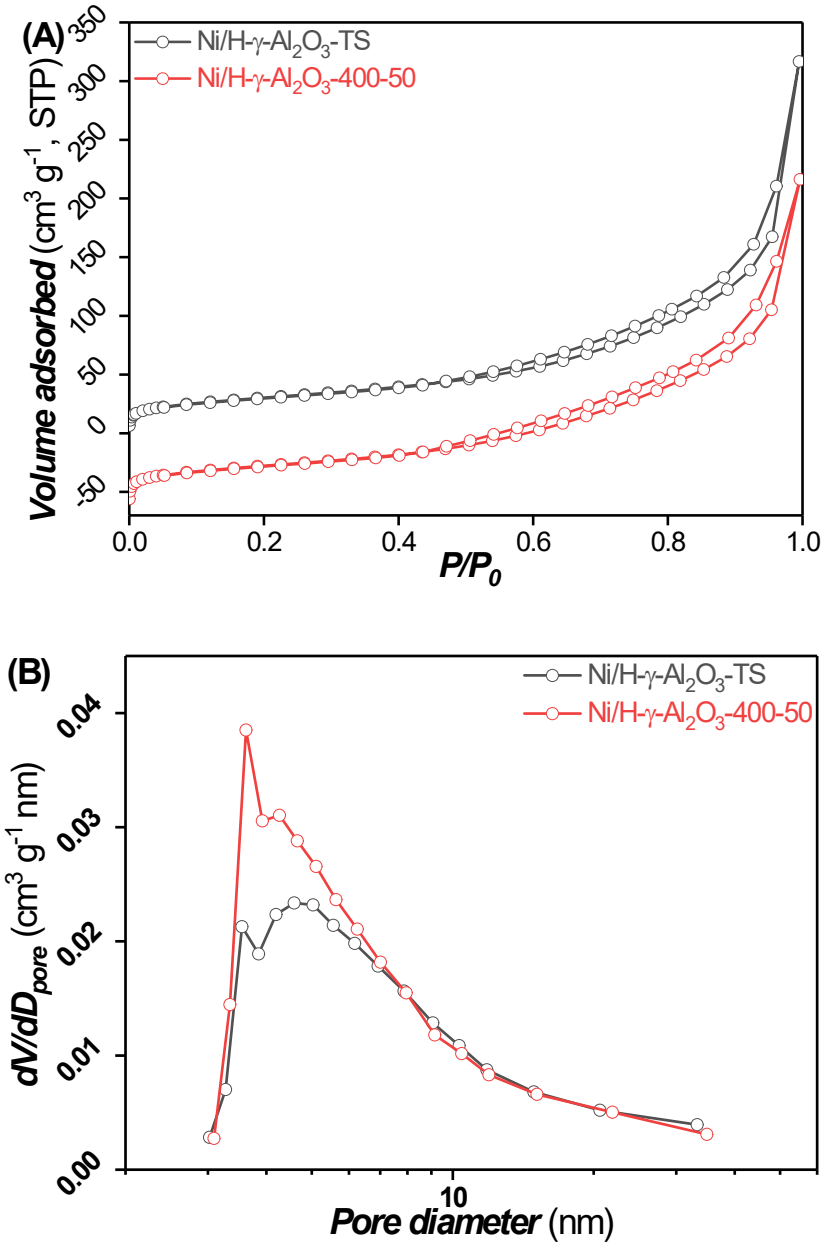

Figure S6. (A) N_2 physisorption isotherms and (B) pore size distributions of the Ni/H-γ-Al_2O_3-TS and Ni/H-γ-Al_2O_3-400-50 samples.

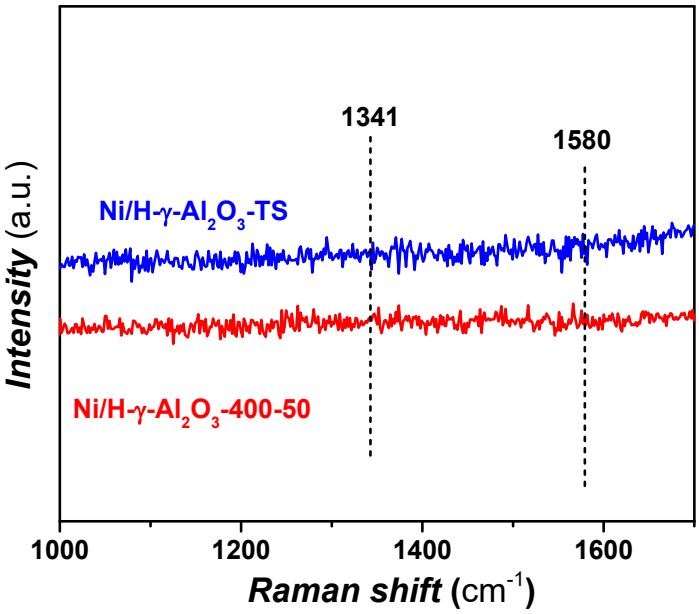

Figure S7. Raman spectra of the Ni/H-γ-Al_2O_3-TS and Ni/H-γ-Al_2O_3-400-50 samples.

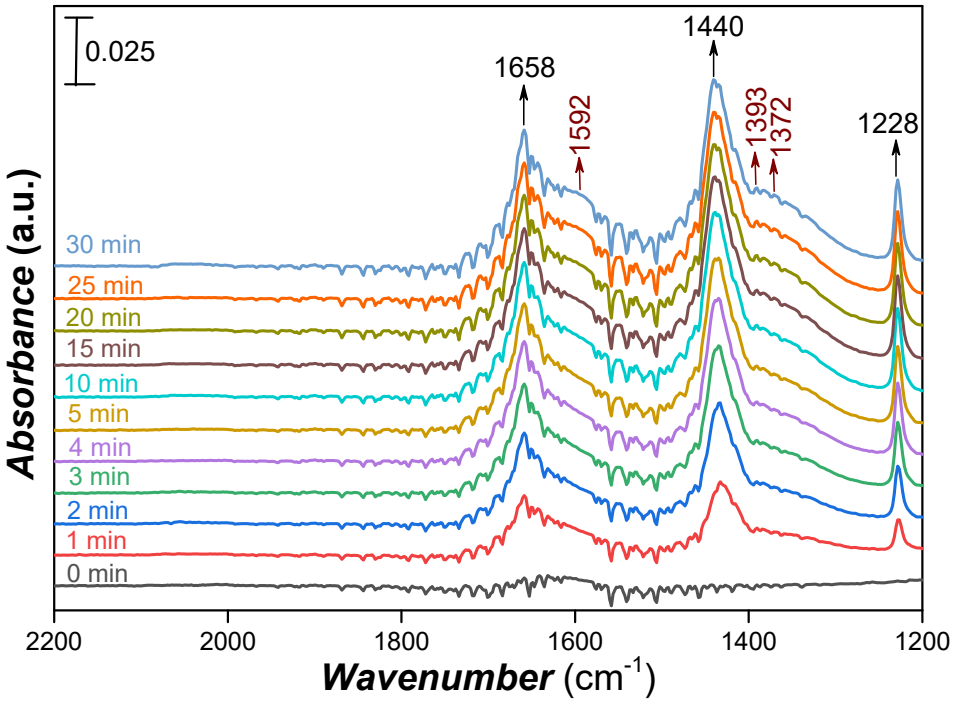

Figure S8. The *in situ* DRIFT spectra recorded in H_2/CO_2 flow on Ni/H-γ-Al_2O_3 catalyst at 50 °C.

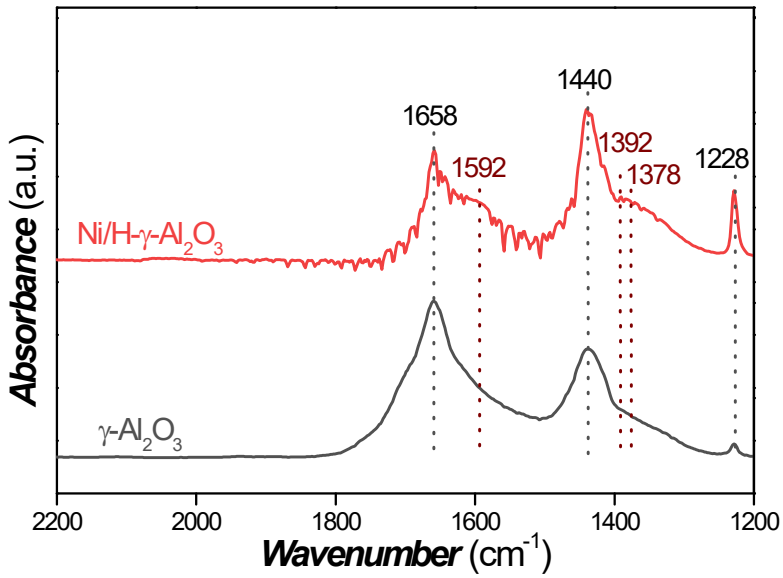

Figure S9. The *in situ* DRIFT spectra recorded in H_2/CO_2 flow for 30 min on γ-Al_2O_3 and Ni/H-γ-Al_2O_3 catalysts at 50 °C.

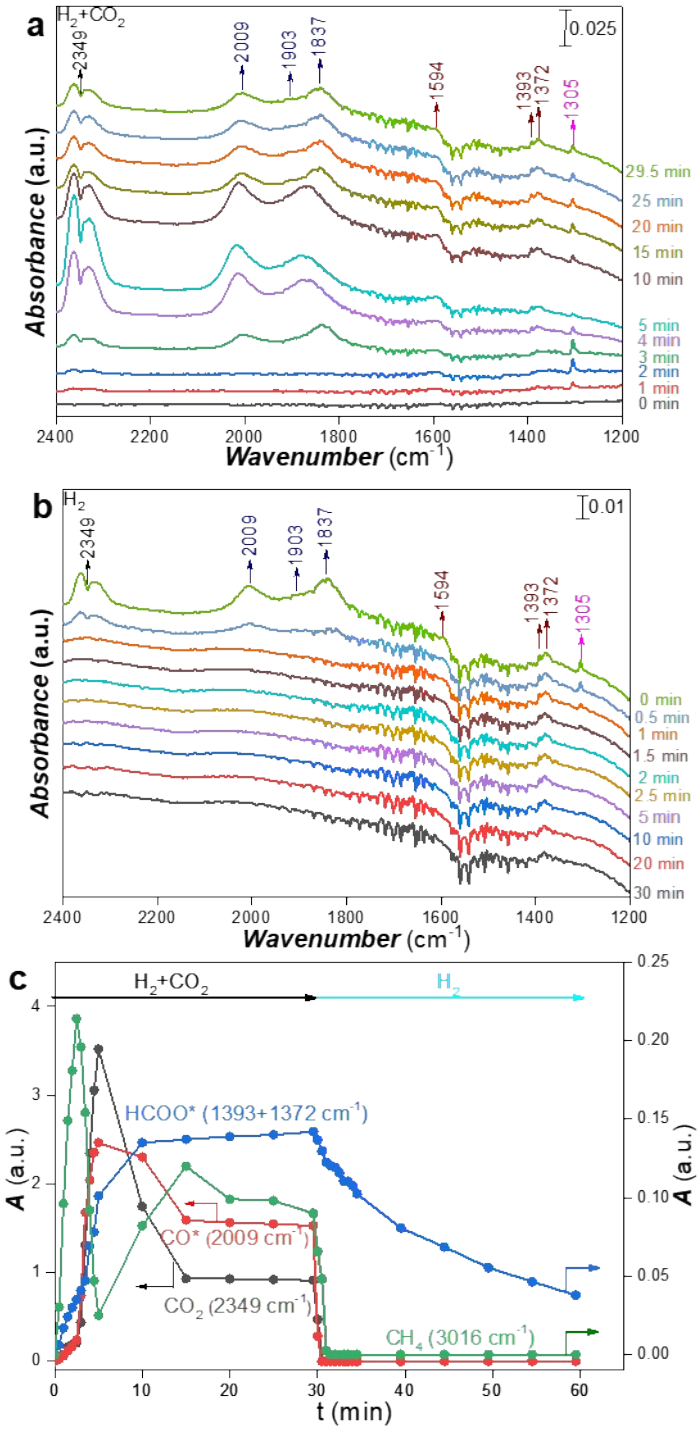

Figure S10. The *in situ* DRIFT spectra recorded in (a) H_2/CO_2 flow, switched into (b) H_2 flow on the Ni/H-γ-Al_2O_3 catalyst at 400 °C. (c) The integrated absorbance (***A***) of related bands versus time extracted from (a) and (b).

Table S1. Activity comparison of catalysts reported in the literature and catalysts reported in this work

Catalysts	Temperature (°C)	H_2/CO	GHSV (ml/g/h)	Conversion of CO_2	Selectivity of CH_4	Refs
Ni/hydroxyapatite	400	4	30000	65.0%	95.0%	1
Ni/CeO_2	400	4	30000	70.0%	95.0%	2
Ni/Al_2O_3	400	4	55000	77%	94.8%	3
Ni/La_2O_3	400	4	20000	72%	96%	4
Ni/Al_2O_3	400	4	9000	50%	90%	5
Ni/Al_2O_3	400	4	480000	60%	90%	6
10%Ni-Ce/Al_2O_3	400	4	15000	69.0%	97.5%	7
Ni/Mg-Al_2O_3	400	4	160000	65%	86%	8
Ni/zeolites	400	4	43000	65.5%	94.2%	9
Ni/ZrO_2	400	4	60000	74.2%	95.0%	10
Ni/CeO_2-Co_3O_4	400	4	3600	60%	94.0%	11
Ni/H-γ-Al_2O_3	400	4	120000	68%	95.0%	This work

1. Z. Boukha, A. Bermejo-López, B. Pereda-Ayo, J. A. González-Marcos and J. R. González-Velasco, *Appl. Catal. B*, 2022, **314**, 121500.
2. G. Varvoutis, M. Lykaki, S. Stefa, V. Binas, G. E. Marnellos and M. Konsolakis, *Appl. Catal. B*, 2021, **297**, 120401.
3. G. Garbarino, D. Bellotti, P. Riani, L. Magistri and G. Busca, *Int. J. Hydrogen Energy*, 2015, **40**, 9171-9182.
4. Y. Dai, M. Xu, Q. Wang, R. Huang, Y. Jin, B. Bian, C. Tumurbaatar, B. Ishtsog, T. Bold and Y. Yang, *Appl. Catal. B*, 2020, **277**, 119271.
5. C. Cerdá-Moreno, A. Chica, S. Keller, C. Rautenberg and U. Bentrup, *Appl. Catal. B*, 2020, **264**, 118546.
6. P. H. Ho, G. S. de Luna, S. Angelucci, A. Canciani, W. Jones, D. Decarolis, F.

Ospitali, E. R. Aguado, E. Rodríguez-Castellón, G. Fornasari, A. Vaccari, A. M. Beale and P. Benito, *Appl. Catal. B*, 2020, **278**, 119256.

7. L. Xu, F. Wang, M. Chen, D. Nie, X. Lian, Z. Lu, H. Chen, K. Zhang and P. Ge, *Int. J. Hydrogen Energy*, 2017, **42**, 15523-15539.
8. E. H. Cho, Y.-K. Park, K. Y. Park, D. Song, K. Y. Koo, U. Jung, W. R. Yoon and C. H. Ko, *Chem. Eng. J.*, 2022, **428**, 131393.
9. I. Graça, L. V. González, M. C. Bacariza, A. Fernandes, C. Henriques, J. M. Lopes and M. F. Ribeiro, *Appl. Catal. B*, 2014, **147**, 101-110.
10. X. Jia, X. Zhang, N. Rui, X. Hu and C.-j. Liu, *Appl. Catal. B*, 2019, **244**, 159-169.
11. F. Hu, C. Jin, R. Wu, C. Li, G. Song, T. Z. H. Gani, K. H. Lim, W. Guo, T. Wang, S. Ding, R. Ye, Z.-H. Lu, G. Feng, R. Zhang and S. Kawi, *Chem. Eng. J.*, 2023, **461**, 142108.